

Lawrence Berkeley National Laboratory

LBL Publications

Title

The electrode–electrolyte interface of Cu via modulation excitation X-ray absorption spectroscopy

Permalink

<https://escholarship.org/uc/item/8cx3175h>

Journal

Energy & Environmental Science, 18(10)

ISSN

1754-5692

Authors

Garcia-Esparza, Angel T
Li, Xiang
Babbe, Finn
et al.

Publication Date

2025-05-20

DOI

10.1039/d5ee01068c

Copyright Information

This work is made available under the terms of a Creative Commons Attribution License, available at <https://creativecommons.org/licenses/by/4.0/>

Peer reviewed

The electrode-electrolyte interface of Cu via modulation excitation X-ray absorption spectroscopy

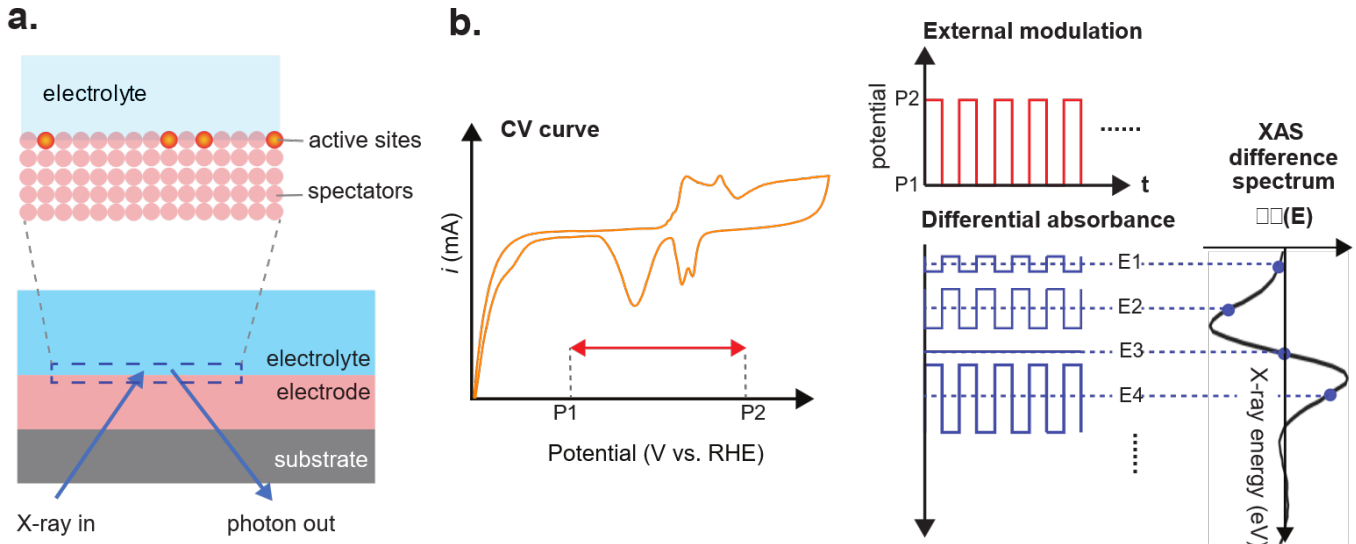
Angel T. Garcia-Esparza,^{a,b} Xiang Li,^{b,c} Finn Babbe,^b Jinkyu Lim,^{a,†} Dean Skoien,^a Philipp S. Simon,^c Junko Yano,^{b,c*} Dimosthenis Sokaras^{a*}

Accessing the electrode-electrolyte interface under operating conditions and capturing time-resolved kinetics challenge electrochemical studies. Copper's interfacial oxidation dynamics remain unclear despite extensive research. Modulation excitation X-ray absorption spectroscopy (ME-XAS) probes Cu in 100 mM KHCO₃ with sub-second sensitivity, revealing hydroxide forming 30±10 ms before Cu₂O at positive potentials (0 to 0.5 V RHE) near open-circuit conditions. At -0.4 to 0.8 V RHE, hydroxide reaches 49% with balanced Cu(I) and Cu(II) oxides. These insights into Cu interfacial redox under intermittent renewable energy operation—relevant to CO₂ electrolyzer durability—enhance our fundamental understanding of electrochemical interfaces.

Electrochemical energy conversions using sustainable energy is a promising solution for the evolution of our fossil fuels-based society.^{1,2} So far, the effects of renewable energy's intermittent working conditions on the redox chemistry of metals at the electrode-electrolyte interface are mostly under-explored and will become key for the successful large-scale implementation of next-generation electrochemical devices.³ In particular, a Cu electrocatalyst is key for the upgrade of CO₂ to fuels and other high-value feedstocks. Cu is the only element capable of the electrocatalytic multi-step conversion of CO₂ or CO to C₂₊ chemicals; however, with low efficiency and selectivity.^{1,4} Furthermore, the durability of Cu-based systems falls significantly short of the thousands of hours of operation required for large-scale deployment.^{5,6} Additionally, the effects of the dynamics of diurnal operation on the interfacial state of Cu at the electrode-electrolyte interface under open circuit potential (OCV) are not well-understood. Hence, the rigorous understanding of the electrochemical redox properties of Cu, its passivation, oxidation kinetics, and corrosion mechanisms are critical to extend the lifetime of electrochemical energy conversion technologies.^{7–10}

Copper's redox properties and behavior in aqueous environments have been the subject of extensive studies.^{7,8,10–29} Using a concentrated NaOH electrolyte, Müller proposed in 1907 that Cu undergoes a series of anodic processes: Cu dissolves to cuprous ions, then transforms to cuprous oxide (Cu₂O), followed by a second dissolution to cupric ions and the evolution of cupric oxide (CuO).⁷ Further studies in alkaline media have been documented using chronopotentiometry^{8,11,12} chronoamperometry,^{21,30} cyclic voltammetry,^{13,17–20,22,23,26–28,31} photoelectrochemical,³² and spectroelectrochemical studies.^{16,19,23} In combination with X-ray diffraction, X-ray photoelectron, Auger, and Raman spectroscopy,^{15,17,19,21,25–29} it is widely recognized that oxides of copper passivate the surface in a pH range of 8–13 under anodic potentials (which is consistent with the Pourbaix diagram).^{33,34} Cu reacts easily with

oxygen-containing electrolytes Cu(110) > Cu(100) > Cu(111).^{19,27,35} When a Cu electrode is anodically polarized in alkaline media, a surface layer of Cu₂O forms through electrosorption of oxygen-containing species on the Cu surface as the first oxidation step.¹⁹ As the anodic potential increases, Cu(OH)₂ and CuO multilayers grow passivating the surface before O₂ generation from water oxidation. Single-crystal studies show hints of OH* coverage, and a subsequent generation of Cu₂O before the evolution of Cu(II) species.^{16,27} Nonetheless, the formation dynamics and the composition of the complex oxide structure at the electro-electrolyte interface remain debatable.



Scheme 1 (a) The scheme shows an electrode-electrolyte interface where the bulk electrode material is subject to an external electric potential to drive an electrochemical reaction at specific active-sites, while most of the atoms are spectators. (b) In the ME-XAS experiment, an external modulation (e.g., electric potentials P1 and P2 in the cyclic voltammogram) drives the system, for example, from a non-faradaic to a Faradaic working state with a specific operating frequency ($1/T$). Only the absorbance of the active species follows the modulation frequency, generating spectral differences as a function of the incident X-ray energy. Thus, the method is sensitive to the changes at the electrochemically active interface.

Capturing the electrode-electrolyte interface has been the subject of intense research efforts for over a century.^{36–41} Probing the surface-active species of bulk electrodes under true working conditions is a challenging task.^{37,39–42} Hard X-ray absorption spectroscopy (>6 keV), due to its element specificity, has been widely used for *in situ* and *operando* electrochemical studies, probing oxidation states, chemical bonding, and coordination under steady-state conditions.^{43–51} However, by probing all atoms of the same element, hard X-rays predominantly provide ensemble-averaged information of the bulk, limiting the detection sensitivity of interfacial phenomena;⁴³ i.e., the active sites signal is typically overwhelmed by the background of spectators. Moreover, in typical *operando* XAS of electrochemical systems, the spectra are obtained at multiple potentials at steady-state conditions (if the catalyst is sufficiently stable for the measurements and have a high enough surface-to-bulk ratio to detect the spectral differences) and cannot access kinetic information. Therefore, it is essential to develop active-site- (or interface) selective methods using X-rays that can be employed upon true operational conditions with temporal resolution (**Scheme 1a**).^{43,52,53}

The modulation excitation (ME) method has been successfully applied across various spectroscopies to isolate and improve the detection of weak signals.^{54,55} This approach involves periodically modulating an external perturbation while synchronizing the detection with the modulation frequency.^{54–60} In electrochemistry, using electric potential as the modulation parameter offers important advantages over steady-state *operando* XAS:^{61,62} (i) it rejects background contributions that do not follow the modulation frequency, effectively enhancing the signal-to-noise ratio, (ii) it follows and isolates signals that respond only to the applied potential, providing greater

interfacial sensitivity, and (iii) it enables access to kinetics information through phase demodulation techniques.^{54–57,59} Herein, we develop and employ ME-XAS to study Cu at an oxygen-free bicarbonate electrolyte interface that capture chemical species' dynamics in the ms timescale under operation conditions. Overall, the approach and the results have universal implications for the fundamental understanding of the redox behavior of Cu and its oxidation mechanism under open circuit potential conditions in aqueous alkaline media.

Scheme 1b summarizes the concept of ME-XAS with potential modulation. In this approach, X-ray absorbance is measured at each incident photon energy, while the applied potential is modulated at a pre-determined frequency between P1 and P2. The X-ray absorbance of the active species responds to the modulation frequency, allowing for the extraction of difference spectra ($\Delta\mu$) as a function of incident X-ray energy. This technique isolates the signals from the minority active sites while effectively filtering out contributions from spectators. Phase-sensitive detection (PSD) is employed for demodulation, providing phase-resolved spectra that reveal the kinetics of the processes at the interface.^{54–57,59} As a result, we obtain time-resolved information on the chemical changes occurring at the electrode-electrolyte interface. Further details regarding the instrumentation and technical protocols are available in the supporting information (**Fig. S1** and **S2**).

Cu electrodes were fabricated via e-beam evaporation on Si_3N_4 X-ray windows. **Figure 1a** shows the electrochemical cyclic voltammetry (CV) characterization of a polycrystalline 100 nm Cu electrode in a flow cell with 10 ml per minute 0.1 M KHCO_3 under Ar saturation to maintain an oxygen-free electrolyte (**Fig. S1**). First, Cu catalyzes the hydrogen evolution reaction (HER) at potentials more negative than -0.4 V_{RHE} (**Fig. 1a**). Second, anodic currents evolved at potentials more positive than 0.3

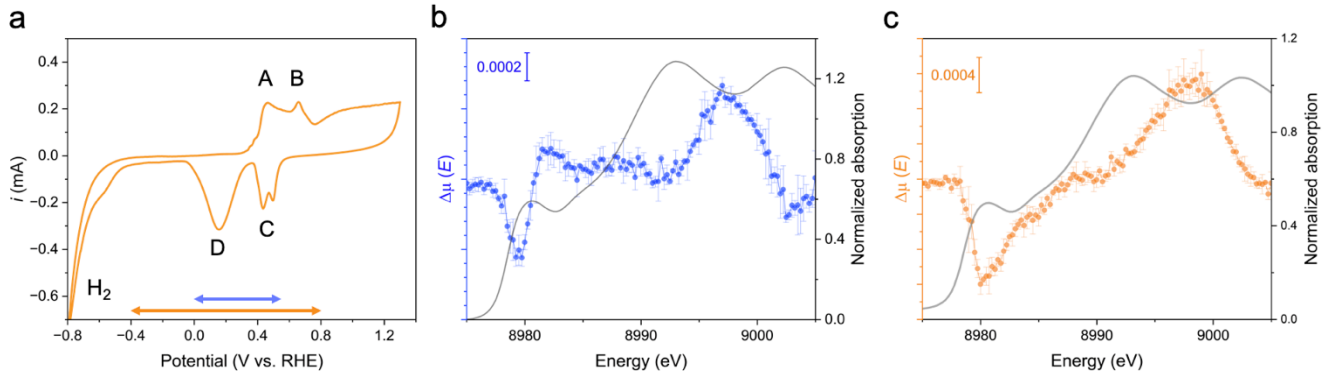


Fig. 1 (a) Cyclic voltammetry of a polycrystalline 100 nm Cu electrode in an electrochemical flow cell with 100 mM $KHCO_3$ (100 mV s $^{-1}$, 10 ml min $^{-1}$, Ar saturation). The anodic redox peaks are highlighted as A and B, and the cathodic redox peaks as C and D. The Cu K-edge ME-XAS of a 100 nm Cu electrode collected under potential modulations between (b) 0 V and 0.5 V, and (c) -0.4 V and 0.8 V vs. the reversible hydrogen electrode (RHE) at 1.3 Hz. The mean spectral difference between the state at (b) 0.5 V_{RHE} or (c) 0.8 V_{RHE} subtracted from the state at 0 V_{RHE} or -0.4 V_{RHE}, respectively, is extracted from three acquisitions with the error bars showing one standard deviation. The normalized Cu K-edge X-ray absorption near-edge structure (XANES) of the electrode held at -0.4 V_{RHE} (metallic spectrum) is shown to highlight the energy regions where the spectral differences are observed.

V_{RHE} . Two minor peaks observed in the anodic scan at 0.35 and 0.38 V_{RHE} are tentatively ascribed to the electrosorption of oxygen species (Fig. 1a, and Fig. S3).^{19,28} The two main anodic peaks at 0.46 V_{RHE} (A) and 0.66 V_{RHE} (B) are commonly assigned to the oxidation of Cu(0) to Cu(I) and then to Cu(II).^{7,8,11,12,18-20,25,26,29} The broad anodic feature above 0.8 V_{RHE} is typically correlated to further converting metallic Cu and Cu(I) into mixed oxidized species (e.g., cupric oxide, copper hydroxide, or a higher state of copper before the water oxidation reaction).^{7,8,11,12,14,18,20,22,23,25,30} Finally, on the cathodic sweep, the observed peaks between 0 and 0.5 V_{RHE} (C, D) are attributed to the reduction of hydroxide to cupric oxide, the reduction from Cu(II) to Cu(I), and the direct complex reduction of Cu(II) and Cu(I) to metallic Cu, respectively.²⁶ The electrochemical characterization of the Cu electrode in the bicarbonate electrolyte is consistent with reported results using alkaline media. Nonetheless, it is challenging to rigorously differentiate and assign the redox steps due to the semiconducting and insulating nature of the formed oxide and hydroxide structures.^{14,17,23,26,29} To this end, we used ME-XAS to interpret the nature and kinetics of the oxidation reaction in detail.

In the ME mode, the applied potential is modulated at 1.3 Hz between two potentials (P1 and P2 in Scheme 1b) while recording the X-ray absorption of the sample for a grid of incident energies along the Cu K-edge region. The 1.3 Hz modulation provides access to the relevant phenomena in sub-second timescales. Two potential windows were explored: 0 to 0.5 V_{RHE} (Fig. 1b), and -0.4 to 0.8 V_{RHE} (Fig. 1c) to probe the oxidation of Cu near open circuit potential conditions. At each incident X-ray energy point, the Cu fluorescence intensity was acquired for at least six modulation cycles with a rate of 100 kHz; these time traces were binned down to 200 Hz giving a final time step of 5 ms (Fig. S2). The difference spectra ($\Delta\mu$) from the Cu K-edge ME-XAS in Figure 1b, c are constructed by subtracting the anodic from the cathodic condition. Cu is in a metallic state under a constant applied potential of -0.4 V_{RHE} (gray line in Fig. 1b, c, and Fig. S4). The first negative peak of the difference spectra with maxima at 8980 eV is related to changes of the XAS

rising edge attributed to dipole-allowed 1s-to-4p transitions, and it indicates the oxidation of Cu.⁶³⁻⁶⁵ A single positive peak at 8982 eV (Fig. 1b), qualitatively resembles a fingerprint that is unique for the formation of Cu_2O (vide infra, Fig. S4b). The broad above-edge feature starting at around 8995 eV is correlated to positive shifts of the main edge of the XAS; mostly related to structural resonances determined by multiple photoelectrons scattering.⁶⁴ Such high energy features are ascribed to the formation of oxygenated Cu species via oxidation, based on the reference spectra of standard samples (Fig. S4). As shown in Figure 1b, c, the ME-XAS can detect spectral changes better than 0.02% in signal differences. Assuming an atomically flat 100 nm Cu, the throughput of the ME-XAS scheme provides the sensitivity to access sub-monolayer (ML) interfacial changes. When considering that the actual surface area is significantly larger due to the morphology of the sputtered electrode and any surface reconstruction mediated by potential modulation, the surface sensitivity of ME-XAS is notably enhanced, making the detection of solid-liquid interfacial phenomena remarkably effective.

Figure 2a, c show the phase-resolved spectra at the Cu K-edge from the two potential windows: 0 to 0.5 V_{RHE} (Fig. 2a), and -0.4 and 0.8 V_{RHE} (Fig. 2c) assuming quasi-reversibility. Spectral differences evolve as a function of the phase in the rising edge energy region between 8977 eV and 8985 eV and on the main white line peak between 8991 and 9005 eV. When the potential window is restricted below the first anodic redox peak A in Fig. 1a (0 to 0.5 V_{RHE}), there are three well-resolved spectral differences centered at 8979.2 eV, 8981.7 eV, and 8997 eV (Fig. 2a). For the wider potential window of -0.4 to 0.8 V_{RHE} , three broad spectral differences with maxima at 8980 eV, 8984.3 eV (shoulder), and 8997.8 eV are obtained (Fig. 2c). These resolved differences arise from the convolution of the disappearance and formation of metallic Cu and multiple oxidized Cu species. Figure 2b, d show the integrated intensity of three energy regions of the demodulated spectra in Fig. 2a, c as a function of their phase-shift: 8977.5-8980 eV (E1), 8981-8983 eV (E2), and

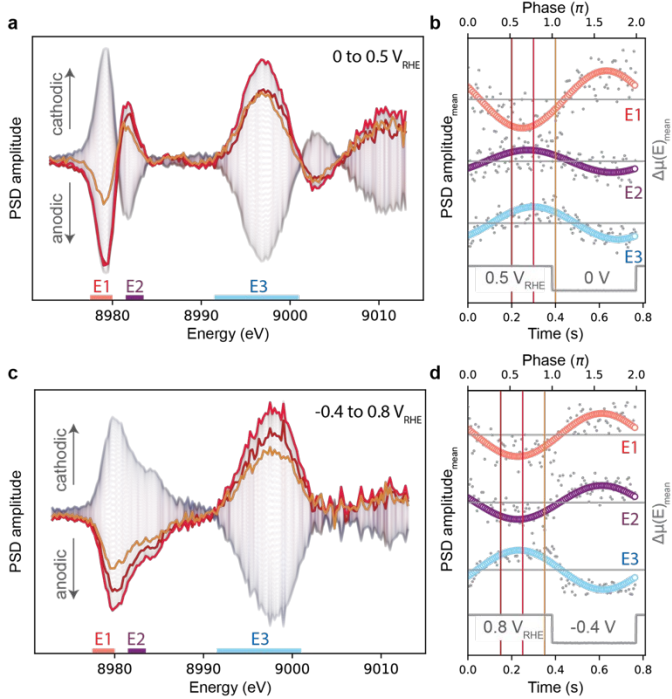


Fig. 3 Phase-resolved spectra of the Cu K-edge ME-XAS from a 100 nm Cu electrode in 100 mM KHCO_3 (10 ml min⁻¹, Ar saturation). The potential of the Cu electrode was modulated at 1.3 Hz between (a, b) 0 V and 0.5 V, and between (c, d) -0.4 V and 0.8 V vs. RHE. (a, c) The spectra show the temporal phase evolution from 0 to 2π . The three energy regions, where the main spectral differences are observed, are highlighted as horizontal bars: 8977.5-8980 eV (E1), 8981-8983 eV (E2), and 8991.5-9001 eV (E3). (b, d) The raw (grey dots), and the phase-resolved data (colored circles) are presented both averaged over the indicated energy intervals (E1-3 in a and c). The square-wave electric potential modulation stimulus is shown as reference. The vertical lines correspond to the phase of the highlighted demodulated spectra in (a) and (c).

8991.5-9001 eV (E3). The scattered points in **Fig. 2b, d** show the mean of the raw data for three periods, and it highlights that the phase shift extracted in the demodulated spectra is consistent with the oscillations observed in the raw data. When the potential is modulated between 0 and 0.5 V_{RHE}, there are time delays between E1, E2, and E3. On the other hand, when the modulated anodic potential is larger at 0.8 V_{RHE}, there is almost no delay among E1, E2, and E3.

Figure 3b-e shows snapshots of the time-dependent demodulated spectra collected from two potential windows, between 0 to 0.5 V_{RHE} (**b, c**), and between -0.4 to 0.8 V_{RHE} (**d, e**). Their linear combination fitting analysis (LCA) using the reference standards in **Figure 3a** are also shown (see also **Fig. S4a**).⁶⁶ The LCA fit was first performed for the entire X-ray absorption near-edge structure (XANES) region (8974-9012 eV) and then for the pre-edge plus rising edge region (8974-8991 eV) using the absorption spectra of all combinations of the reference standards (**Fig. 3 b-e top**, and **Figs. S5-S7**).

For the potential range between 0 to 0.5 V_{RHE}, the LCA of the PSD-resolved spectra shows the early formation of Cu(II) with Cu(I) on the surface of Cu under mild anodic potential similar to OCV conditions (200 ms in **Fig. 3b** and **Fig. S5**). The spectral features in the pre-edge and rising edge region (E1 and E2 region in **Fig. 3b,c**) require the inclusion of a fraction of Cu(II) species, alongside the predominantly identified Cu₂O

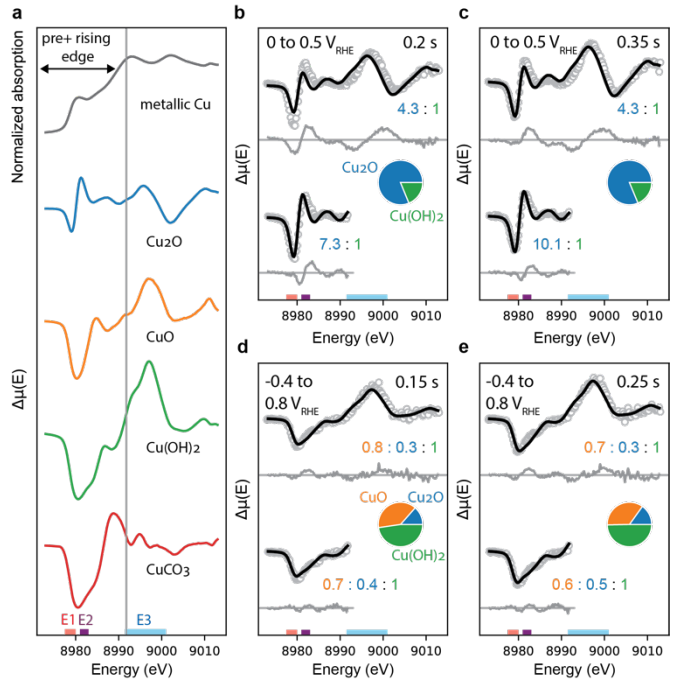


Fig. 2 Linear combination fitting analysis (LCA) of the phase-resolved Cu K-edge ME-XAS. (a) The difference spectra of the Cu standards are used as references for LCA, by subtracting the steady-state metallic Cu spectrum collected at -0.4 V_{RHE}. (b-e) LCA fittings (black solid lines) at (b) 200 ms and (c) 350 ms with a potential modulation between 0 to 0.5 V_{RHE}; and at (d) 150 ms and (e) 250 ms between -0.4 and 0.8 V_{RHE} (1.3 Hz, 100 nm Cu, 100 mM KHCO_3 , 10 ml min⁻¹, Ar saturation). The most abundant species within statistical error are included in the pie charts, the extracted relative amounts are displayed, and the residual of the fit is presented. Two energy ranges were attempted for the fit: the full range from 8974 to 9012 eV, and a smaller pre-edge plus rising edge range fit done between 8974-8991 eV (shown as a gray vertical line in a).

component. Among the available Cu(II) reference spectra, the inclusion of either Cu(OH)₂ or CuO with Cu₂O produced fits of similar statistical quality (**Fig. S7**). It is however challenging to resolve the precise identity of the Cu(II) species using the bulk Cu reference standards: CuO and Cu(OH)₂. While the residual value shows a minor improvement with CuO, the fit quality is similar and, in both cases, they miss a feature between 8980 and 8985 eV at earlier time points (200 and 300 ms in **Fig. S5** and **S7**). We postulate that this is because the reference standards currently available are bulk structures, while the surface species we experimentally capture here likely have geometric distortions that differ from the bulk-like motif. Overall, we ascribe the Cu(II) component to a hydroxide-like structure based on the literature and previous spectroscopic studies in alkaline media (≥ 10 mM KOH or NaOH, pH ≥ 12).^{19,28,67,68}

The formation of O* and OH* species has been previously proposed as the initial step in anodic oxidation of the Cu electrode's surface under alkaline conditions. This is consistent with the peaks observed in our CV in the Ar-saturated carbonate electrolyte near 0.4 V_{RHE} (**Fig. 1** and **Fig. S3**). Therefore, based on the literature, the experimental CV traces, and the LCA of the PSD-resolved spectra, we assigned the Cu(OH)₂ reference standard as the likely candidate to best describe the spectra. In the potential step from 0 to 0.5 V_{RHE} at a delay of 200 ms, the fit

of the full XANES region shows values of 81% Cu₂O and 19% Cu(OH)₂ (**Fig. 3b, top**). A slight increase of Cu₂O was observed in the later spectrum (350 ms), with an improved fit quality (**Fig. 3c, top**). Under the extended potential range (~0.4 to 0.8 V_{RHE}), the relative amount of Cu(I) decreased to a mean value of \approx 18%, and the Cu(II) increased in the form of \approx 49% Cu(OH)₂ and \approx 34% CuO; exhibiting a similar composition throughout the full phase cycle (**Fig. 3d, e**). Notably, when attempting to fit the full energy range, the fit quality is reasonable but unsatisfactory; particularly for the 0 to 0.5 V_{RHE} data (**Fig. 3b, c**). When the fitting range is limited to the pre-edge and rising edge region between 8974–8991 eV, the fit quality improves, showing a 7.3:1 and 11.5:1 ratio of Cu₂O:Cu(OH)₂ after 200 and 350 ms, respectively (**Fig. 3b, c bottom**, and **Fig. S7**). On the other hand, no significant improvement was observed for the –0.4 to 0.8 V_{RHE} data (**Fig. 3d, e bottom**).

As described above, there are clear phase shifts among the spectral components (**Fig. 2b**) and composition changes of the oxygenated Cu species (**Fig. 3b, c**) during the 0 to 0.5 V_{RHE} cycle. No significant changes were observed during the –0.4 to 0.8 V_{RHE} cycle after 30 ms, and any evolution of these components falls below the time resolution achievable with the chosen modulation frequency. **Figure 4a top** shows that during the 0 to 0.5 V_{RHE} cycle the demodulated experimental data exhibits a time-delay of 40 and 55±10 ms for the rise of E2 and E3 with respect to E1. **Figure 4a (bottom)** is the temporal evolution of the LCA components from the full spectrum fit (8974–9012 eV). The integrated intensity of the E1, E2, and E3 regions of the full fit is overlayed as solid lines in **Fig. 4a (top)** that indicates a large discrepancy in the E1 and E2 regions. On the contrary, when limiting the LCA fit to the pre-edge and rising edge energy range, the fit successfully captures the phase shift between the E1 and E2 features (**Fig. 4b top**). The E1 feature arises from the differences of Cu₂O and Cu(II) species from metallic Cu, while the E2 feature is unique in Cu₂O (see **Fig. 3a**), both regions sensitive to the electronic structural changes of Cu.^{64,65} The E3 region, on the other hand, arises likely due to the oxygenation of the lattice.⁶⁴

The early formation of a minor fraction of Cu(II) species is evidenced by the peak maxima of the E1 region prior to that of E2. While the kinetic evolution in **Figure 4** can be described with either Cu(OH)₂ (**Fig. 4b**) or CuO (**Fig. S8**), we ascribed this to Cu(OH)₂ as discussed above. The extracted phase-shift of 30±10 ms between the LCA components (**Fig. 4b bottom**), indicates that a hydroxide adsorbate evolves at the early stage of the oxidation of Cu before the formation of Cu₂O at the interface of metallic Cu and the electrolyte.

In the literature, Droog et al. suggested that the electrosorption of oxygen species precedes the formation of a surface Cu₂O layer in 1 M NaOH.¹⁹ Pyun and Park proposed the formation of hydroxides on the electrode's surface upon anodic polarization in 0.1 M KOH. In-situ STM,⁶⁷ and surface-enhanced Raman spectroscopy⁶⁸ proposed the formation of OH* (700 cm⁻¹ Raman band) with ca. 0.2 ML coverage on Cu(111) at more negative potentials than the formation of Cu₂O in 0.1 M NaOH. Recently, Bodappa et al. decorated Au/SiO₂ core-shell nanoparticles on Cu(111) and recorded two Raman bands at

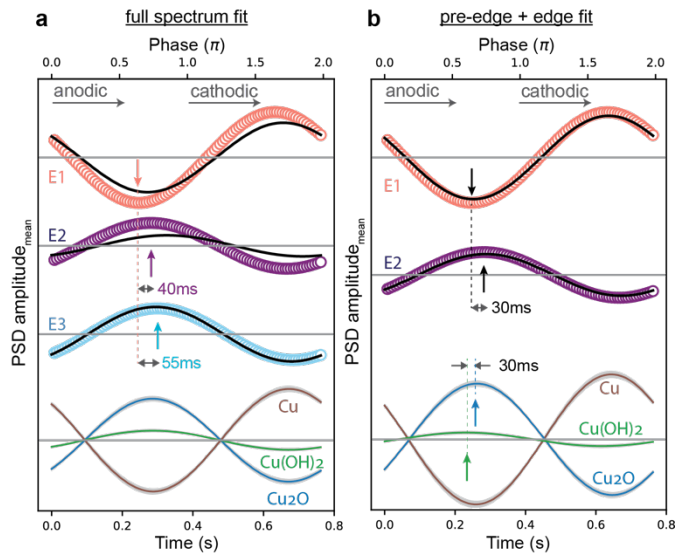


Fig. 4 The temporal evolution of the phase-resolved Cu K-edge ME-XAS spectral features, when the potential of the Cu electrode is modulated between 0 to 0.5 V_{RHE}. In the **top**, the signals (colored circles) are extracted from the integration of the spectral intensity of the defined energy regions (see Fig. 2a,c). The black solid lines show the integrated intensity of the same energy regions obtained from the linear combination fitting analysis (LCA) shown in the **bottom**. The gray areas around the amplitudes of each species spectrum represent the fit error. (**a**) The full spectrum fit was done between 8974–9012 eV, and (**b**) the pre-edge plus edge fit was done between 8974–8991 eV. The arrows indicate the position of the maximum intensity.

535 and 680 cm⁻¹ in 0.01 M KOH (\leq 0.1 V_{RHE}). Based on DFT, they assigned the peaks to the top site OH* stretching mode and the bending mode of OH*, respectively.²⁸ Our current ME-XAS study provides experimental evidence of the early formation of Cu(II) species. Based on the CV, the LCA, and the literature, we propose a surface copper hydroxide forming 40±10 ms after the 0.5 V_{RHE} anodic trigger. Then, Cu₂O evolves 30±10 ms later (**Fig. 4b bottom**). Finally (\geq 200 ms), Cu₂O dominates the composition accompanied by further oxygenation and restructuring of the lattice when the potential is limited from 0 to 0.5 V_{RHE} in polycrystalline Cu in Ar-saturated 0.1 M KHCO₃ (**Fig. 4b**, and **Scheme 2**). The early appearance of OH* is also consistent with the thermodynamic expectations calculated by Protopopoff and Marcus.⁶⁹ When the applied potential exceeds the second anodic peak B ($>$ 0.65 V_{RHE}, **Fig. 1a**), the polarization drives the kinetics of the system towards the rapid formation of Cu(II) species (\geq 30 ms), mostly in the form of Cu(OH)₂ accompanied by CuO via the consumption of metallic Cu and Cu₂O (**Fig. 2d**, and **Fig. 3d, e**).

Conclusions

In this work we developed and applied a ME-XAS to study the electrode-electrolyte interface of Cu in an oxygen-free bicarbonate electrolyte. The PSD of the Cu K-edge ME-XAS revealed insights into the early oxidation of Cu with sub-second resolution under applied potentials similar to open circuit conditions relevant for diurnal start/stop operations. Metallic Cu oxidizes to Cu(I) through hydroxide that developed 30±10 ms earlier. Then, Cu(OH)₂ and CuO evolve and grow under mild anodic potential with the hydroxide phase dominating the

formation kinetics. ME-XAS provides a detailed understanding of the oxidation dynamics of Cu in aqueous alkaline conditions, contributing to the fundamental knowledge of copper's redox properties that is essential for energy conversion and microelectronics technologies. The demonstrated methodology can also significantly impact the design, assessment, and suitability of Accelerated Stress Testing (AST) protocols, using synchronized voltage or current periodic profiles to study corrosion, durability, and performance. The challenging study of heterogeneous interfaces was addressed using the unprecedented sensitivity of ME-XAS to detect subtle chemical changes under real operational conditions. This methodology provides time-resolved insights into dynamic interfacial processes, opening new avenues for understanding critical electrochemical reactions and other interfacial phenomena.

Broader context

Electrochemical reactions at electrode-electrolyte interfaces drive catalysis and energy technologies, yet probing these interfaces under operating conditions with kinetic detail has long been elusive, often obscured by ensemble-averaged information. Our research uses modulation excitation X-ray absorption spectroscopy (ME-XAS) to examine copper—a CO₂ conversion catalyst—revealing dynamic surface redox during renewable energy intermittency (p. 1–8). This sensitivity to surface-specific and time-resolved changes transcends traditional limits, offering unprecedented insight into electrocatalyst behavior. These advances can push forward fundamental catalysis and energy science research by resolving rapid interfacial processes. The ability to track kinetics and intermediates may now unlock questions of catalyst efficiency, selectivity and durability across electrochemical reactions, from energy devices, such as electrolyzers, to broader electrochemical systems. For applications, it informs material behavior under practical stressors; for basic science, it captures elusive surface states, enhancing understanding of reaction mechanisms. This versatility impacts diverse fields—fuel cells, electrolyzers, batteries and beyond—by accessing information on electrochemical interfaces without bulk interference. As catalysis and energy research target sustainable solutions, the presented approach ability to capture true surface dynamics under operating conditions enable innovation across electrochemical technologies, linking basic science discoveries to practical challenges in energy conversion and storage system.

Author contributions

A.T.G-E. designed and performed experiments, analyzed data, prepared figures, drafted original manuscript. X.L. designed and performed experiments, analyzed early data. F.B. prepared and characterized samples. J.L. performed experiments. D.Sk. performed experiments, processed data, developed analysis software, edited manuscript. P.S.S. performed experiments, analyzed data, prepared figures, edited manuscript. J.Y. and D.S.

conceived methodology, designed and performed experiments, allocated resources, supervised research, edited manuscript.

Conflicts of interest

There are no conflicts to declare.

Data availability

The data supporting this article have been included as part of the ESI.

Acknowledgements

Use of the SSRL-SLAC National Accelerator Laboratory, was supported by the U.S. DOE, Office of Science, Office of Basic Energy Sciences under Contract No. DE-AC02-76SF00515. This material is based on work performed by the Liquid Sunlight Alliance, which is supported by the U.S. Department of Energy, Office of Science, Office of Basic Energy Sciences, Fuels from Sunlight Hub under Award Number DE-SC0021266. The phase sensitive data analysis was supported by the Clean Energy Manufacturing Program, U.S. DOE, Office of Science, Office of Basic Energy Sciences, Chemical Sciences, Geosciences, and Biosciences Division, in under contract no. DE-AC0205CH11231 (P. S. and J. Y.).

Notes and references

- Y. Hori, *Electrochemical CO₂ Reduction on Metal Electrodes*, 2008, vol. 42.
- J. B. Greenblatt, D. J. Miller, J. W. Ager, F. A. Houle and I. D. Sharp, *Joule*, 2018, **2**, 381–420.
- A. A. Samu, A. Kormányos, E. Kecsenovity, N. Szilágyi, B. Endrődi and C. Janáky, *ACS Energy Lett*, 2022, **7**, 1859–1861.
- S. Nitopi, E. Bertheussen, S. B. Scott, X. Liu, A. K. Engstfeld, S. Horch, B. Seger, I. E. L. Stephens, K. Chan, C. Hahn, J. K. Nørskov, T. F. Jaramillo and I. Chorkendorff, *Chem Rev*, 2019, **119**, 7610–7672.
- H. Wu, H. Yu, Y. L. Chow, P. A. Webley and J. Zhang, *Advanced Materials*, DOI:10.1002/adma.202403217.
- J. A. Rabinowitz and M. W. Kanan, *Nat Commun*, 2020, **11**, 10–12.

- 7 A. Hickling and D. Taylor, *Transactions of the Faraday Society*, 1948, **44**, 262–268.
- 8 S. E. S. El Wakkad and S. H. Emara, *Journal of the Chemical Society (Resumed)*, 1953, 3508–3512.
- 9 S. Mu, H. Lu, Q. Wu, L. Li, R. Zhao, C. Long and C. Cui, *Nat Commun*, 2022, **13**, 1–8.
- 10 J. Peng, B. Chen, Z. Wang, J. Guo, B. Wu, S. Hao, Q. Zhang, L. Gu, Q. Zhou, Z. Liu, S. Hong, S. You, A. Fu, Z. Shi, H. Xie, D. Cao, C. J. Lin, G. Fu, L. S. Zheng, Y. Jiang and N. Zheng, *Nature*, 2020, **586**, 390–394.
- 11 A. M. S. El Din and F. M. A. El Wahab, *Electrochim Acta*, 1964, **9**, 113–121.
- 12 M. J. Dignam and D. B. Gibbs, *Can J Chem*, 1970, **48**, 1242–1250.
- 13 N. A. Hampson, J. B. Lee and K. I. Macdonald, *Journal of Electroanalytical Chemistry*, 1971, **32**, 165–173.
- 14 J. Kunze, V. Maurice, L. H. Klein, H. H. Strehblow and P. Marcus, *Corros Sci*, 2004, **46**, 245–264.
- 15 H. H. Strehblow and B. Titze, *Electrochim Acta*, 1980, **25**, 839–850.
- 16 C. H. Pyun, C. Zhang and S. M. Park, *Electrochemical Society Extended Abstracts*, 1985, **85-2**, 74–75.
- 17 J. B. He, D. Y. Lu and G. P. Jin, *Appl Surf Sci*, 2006, **253**, 689–697.
- 18 J. Ambrose, R. G. Barradas and D. W. Shoesmith, *Journal of Electroanalytical Chemistry*, 1973, **47**, 47–64.
- 19 J. M. M. Droog, C. A. Alderliesten, P. T. Alderliesten and G. A. Bootsma, *J Electroanal Chem*, 1980, **111**, 61–70.
- 20 B. Miller, *J Electrochem Soc*, 1969, **116**, 1675.
- 21 D. W. Shoesmith, S. Sunder, M. G. Bailey, G. J. Wallace and F. W. Stanchell, *Journal of Electroanalytical Chemistry*, 1983, **143**, 153–165.
- 22 S. M. Abd el Haleem and B. G. Ateya, *Journal of Electroanalytical Chemistry*, 1981, **117**, 309–319.
- 23 S. Dong, Y. Xie and G. Cheng, *Electrochim Acta*, 1992, **37**, 17–22.
- 24 M. Metikoš-Huković, R. Babić and I. Paić, *J Appl Electrochem*, 2000, **30**, 617–624.
- 25 Y. Deng, A. D. Handoko, Y. Du, S. Xi and B. S. Yeo, *ACS Catal*, 2016, **6**, 2473–2481.
- 26 S. Nakayama, T. Kaji, M. Shibata, T. Notoya and T. Osakai, *J Electrochem Soc*, 2007, **154**, C1.
- 27 J. H. Baricuatro, C. B. Ehlers, K. D. Cummins, M. P. Soriaga, J. L. Stickney and Y. G. Kim, *Journal of Electroanalytical Chemistry*, 2014, **716**, 101–105.
- 28 N. Bodappa, M. Su, Y. Zhao, J. B. Le, W. M. Yang, P. Radjenovic, J. C. Dong, J. Cheng, Z. Q. Tian and J. F. Li, *J Am Chem Soc*, 2019, **141**, 12192–12196.
- 29 M. Scherzer, F. Girgsdies, E. Stotz, M. G. Willinger, E. Frei, R. Schlögl, U. Pietsch and T. Lunkenbein, *Journal of Physical Chemistry C*, 2019, **123**, 13253–13262.
- 30 D. W. Shoesmith, T. E. Rummery, D. Owen and W. Lee, *J Electrochem Soc*, 1976, **123**, 790–799.
- 31 N. A. Hampson, R. J. Latham, J. B. Lee and K. I. Macdonald, *Journal of Electroanalytical Chemistry*, 1971, **31**, 57–62.
- 32 A. T. Garcia-Esparza, K. Limkailassiri, F. Leroy, S. Rasul, W. Yu, L. Lin and K. Takanabe, *J Mater Chem A Mater*, 2014, **2**, 7389.

- 33 L. N. Walters, L. F. Huang and J. M. Rondinelli, *Journal of Physical Chemistry C*, 2021, **125**, 14027–14038.
- 34 B. Beverskog and I. Puigdomenech, *J Electrochem Soc*, 1997, **144**, 3476–3483.
- 35 R. N. Lee and H. E. Farnsworth, *Surf Sci*, 1965, **3**, 461–479.
- 36 H. L. F. von Helmholtz, *Ann Phys*, 1853, **89**, 211.
- 37 J. J. Velasco-Velez, C. H. Wu, T. A. Pascal, L. F. Wan, J. Guo, D. Prendergast and M. Salmeron, *Science* (1979), 2014, **346**, 831–834.
- 38 J. M. Dawlaty, S. Perkin, M. Salanne and A. P. Willard, *Journal of Chemical Physics*, 2023, **159**, 2021–2024.
- 39 J. E. N. Swallow, M. W. Fraser, N. J. H. Kneusels, J. F. Charlton, C. G. Sole, C. M. E. Phelan, E. Björklund, P. Bencok, C. Escudero, V. Pérez-Dieste, C. P. Grey, R. J. Nicholls and R. S. Weatherup, *Nat Commun*, DOI:10.1038/s41467-022-33691-1.
- 40 M. Favaro, B. Jeong, P. N. Ross, J. Yano, Z. Hussain, Z. Liu and E. J. Crumlin, *Nat Commun*, 2016, **7**, 1–8.
- 41 C. H. Wu, T. A. Pascal, A. Baskin, H. Wang, H. T. Fang, Y. S. Liu, Y. H. Lu, J. Guo, D. Prendergast and M. B. Salmeron, *J Am Chem Soc*, 2018, **140**, 16237–16244.
- 42 C. Y. Li, J. B. Le, Y. H. Wang, S. Chen, Z. L. Yang, J. F. Li, J. Cheng and Z. Q. Tian, *Nat Mater*, 2019, **18**, 697–701.
- 43 B. Lassalle-Kaiser, S. Gul, J. Kern, V. K. Yachandra and J. Yano, *J Electron Spectros Relat Phenomena*, 2017, **221**, 18–27.
- 44 A. T. Garcia-Esparza, S. Park, H. Abroshan, O. A. Paredes Mellone, J. Vinson, B. Abraham, T. R. Kim, D. Nordlund, A. Gallo, R. Alonso-Mori, X. Zheng and D. Sokaras, *ACS Nano*, 2022, **16**, 6725–6733.
- 45 X. Shi, H.-J. Peng, T. J. P. Hersbach, Y. Jiang, Y. Zeng, J. Baek, K. T. Winther, D. Sokaras, X. Zheng and M. Bajdich, *ACS Energy Lett*, 2022, **7**, 2228–2235.
- 46 M. Reinhard, A. Gallo, M. Guo, A. T. Garcia-Esparza, E. Biasin, M. Qureshi, A. Britz, K. Ledbetter, K. Kunnus, C. Weninger, T. van Driel, J. Robinson, J. M. Glownia, K. J. Gaffney, T. Kroll, T. C. Weng, R. Alonso-Mori and D. Sokaras, *Nat Commun*, 2023, **14**, 1–11.
- 47 S. H. Shim, B. Ko, D. Sokaras, B. Nagler, H. J. Lee, E. Galtier, S. Glenzer, E. Granados, T. Vinci, G. Fiquet, J. Dolinschi, J. Tappan, B. Kulka, W. L. Mao, G. Morard, A. Ravasio, A. Gleason and R. Alonso-Mori, *Sci Adv*, DOI:10.1126/SCIADV.ADI6153.
- 48 M. C. Cendejas, O. A. Paredes Mellone, U. Kurumbail, Z. Zhang, J. H. Jansen, F. Ibrahim, S. Dong, J. Vinson, A. N. Alexandrova, D. Sokaras, S. R. Bare and I. Hermans, *J Am Chem Soc*, 2023, **145**, 25686–25694.
- 49 T. J. P. Hersbach, A. C. Garcia, T. Kroll, D. Sokaras, M. T. M. Koper and A. T. Garcia-Esparza, *ACS Catal*, 2021, **11**, 9904–9915.
- 50 C. Kuai, Y. Zhang, D. Wu, D. Sokaras, L. Mu, S. Spence, D. Nordlund, F. Lin and X. W. Du, *ACS Catal*, 2019, **9**, 6027–6032.
- 51 D. Friebel, M. W. Louie, M. Bajdich, K. E. Sanwald, Y. Cai, A. M. Wise, M. J. Cheng, D. Sokaras, T. C. Weng, R. Alonso-Mori, R. C. Davis, J. R. Bargar, J. K. Nørskov, A. Nilsson and A. T. Bell, *J Am Chem Soc*, 2015, **137**, 1305–1313.
- 52 J. Song, Z. X. Qian, J. Yang, X. M. Lin, Q. Xu and J. F. Li, *ACS Energy Lett*, 2024, **9**, 4414–4440.
- 53 E. Pastor, Z. Lian, L. Xia, D. Ecija, J. R. Galán-Mascarós, S. Barja, S. Giménez, J. Arbiol, N.

- López and F. P. García de Arquer, *Nat Rev Chem*, 2024, **8**, 159–178.
- 54 V. Marchionni, D. Ferri, O. Kröcher and A. Wokaun, *Anal Chem*, 2017, **89**, 5801–5809.
- 55 P. Müller and I. Hermans, *Ind Eng Chem Res*, 2017, **56**, 1123–1136.
- 56 A. Urakawa, D. Ferri and R. J. G. Nuguid, in *Handbook of Advanced Catalyst Characterization*, Springer, 2023, pp. 967–977.
- 57 J. Weyel, L. Schumacher, M. Ziembka, M. Pfeiffer and C. Hess, *Acc Chem Res*, DOI:10.1021/acs.accounts.4c00351.
- 58 P. D. Srinivasan, B. S. Patil, H. Zhu and J. J. Bravo-Suárez, *React Chem Eng*, 2019, **4**, 862–883.
- 59 A. Urakawa, T. Bürgi and A. Baiker, *Chem Eng Sci*, 2008, **63**, 4902–4909.
- 60 P. K. Routh, E. Redekop, S. Prodinger, J. E. S. van der Hoeven, K. R. G. Lim, J. Aizenberg, M. Nachtegaal, A. H. Clark and A. I. Frenkel, *Nat Commun*, 2024, **15**, 1–10.
- 61 S. Czioska, A. Boubnov, D. Escalera-López, J. Geppert, A. Zagalskaya, P. Röse, E. Saraçi, V. Alexandrov, U. Krewer, S. Cherevko and J. D. Grunwaldt, *ACS Catal*, 2021, **11**, 10043–10057.
- 62 W. Xu, G. Zhang, H. Shou, J. Zhou, S. Chen, S. Chu, J. Zhang and L. Song, *J Synchrotron Radiat*, 2022, **29**, 1065–1073.
- 63 M. R. Zoric, P. Basera, L. D. Palmer, A. Aitbekova, N. Powers-Riggs, H. Lim, W. Hu, A. T. Garcia-Esparza, H. Sarker, F. Abild-Pedersen, H. A. Atwater, S. K. Cushing, M. Bajdich and A. A. Cordones, *ACS Nano*, DOI:10.1021/acsnano.4c02088.
- 64 L. shan Kau, D. J. Spira-solomon, J. E. Spira-solomon-penner-hahn, K. O. Hodgson and E. I. Solomon, *J Am Chem Soc*, 1987, **109**, 6433–6442.
- 65 J. Rudolph and C. R. Jacob, *Inorg Chem*, 2018, **57**, 10591–10607.
- 66 A. Gaur, D. Shrivastava and K. Joshi, *J Phys Conf Ser*, DOI:10.1088/1742-6596/190/1/012084.
- 67 V. Maurice, H. H. Strehblow and P. Marcus, *Surf Sci*, 2000, **458**, 185–194.
- 68 S. Härtinger, B. Pettinger and K. Doblhofer, *Journal of Electroanalytical Chemistry*, 1995, **397**, 335–338.
- 69 E. Protopopoff and P. Marcus, *Electrochim Acta*, 2005, **51**, 408–417.